Microbiota-derived indole-3-propionic acid reprograms bone marrow stem cell fate via PPARγ suppression to rescue osteoporosis

JINWU BAI[1,2], RUIDENG WANG[3], JIXING FAN[1,2], SHILONG SU[1,2], GAO SI[1,2], QINYONG YOU[1,2], AO SUN[1,2], DAOLE HU[1,2], SHAN GAO[1,2], YANG LV[1,2] and FANG ZHOU[1,2]

[1]Department of Orthopedics, Peking University Third Hospital, Beijing 100191, P.R. China;
[2]Beijing Key Laboratory of Advanced Bioadaptable Orthopedic Implants, Peking University Third Hospital, Beijing 100191, P.R. China;
[3]Department of Orthopedics, Shenzhen Traditional Chinese Medicine Hospital, Shenzhen, Guangdong 518032, P.R. China

Received March 20, 2026; Accepted May 22, 2026

DOI: 10.3892/ijmm.2026.5879

Abstract. Osteoporosis (OP) is increasingly recognised as a disorder driven by impaired lineage allocation of bone marrow stromal cells (BMSCs), characterised by a shift from osteogenesis toward adipogenesis under conditions such as oestrogen deficiency and oxidative stress. Although gut microbiota-derived metabolites have emerged as critical regulators of skeletal homeostasis, their direct role in BMSC fate determination remains poorly understood. In the present study, indole-3-propionic acid (IPA) was identified, a metabolite produced by *Clostridium sporogenes*, as a key regulator of bone-fat balance. Integrative analyses combining 16S rRNA sequencing, metabolomics, transcriptomics and functional assays revealed that IPA levels were significantly reduced in ovariectomised mice and positively correlated with bone mass. Functionally, IPA protected BMSCs from oxidative stress-induced apoptosis, restored osteogenic capacity, and suppressed adipogenic differentiation. Mechanistically, RNA sequencing and molecular docking analyses demonstrated that IPA modulates the peroxisome proliferator-activated receptor gamma (PPARγ) signalling pathway, thereby reprogramming BMSC lineage commitment. *In vivo*, oral administration of IPA markedly improved trabecular bone microarchitecture, enhanced bone formation, and corrected marrow adiposity without detectable systemic toxicity. Collectively, the present findings identified IPA as a previously under-recognised microbiota-derived metabolite that maintains skeletal homeostasis by restoring the osteogenic-adipogenic balance through suppression of PPARγ signalling. The present study uncovers a mechanistic link between gut microbial metabolism and BMSC fate regulation and highlights IPA as a promising therapeutic candidate for OP.

Correspondence to: Professor Fang Zhou or Professor Yang Lv, Department of Orthopedics, Peking University Third Hospital, 49 Garden North Road, Haidian, Beijing 100191, P.R. China
E-mail: zhouf@bjmu.edu.cn
E-mail: lvyang42@126.com

Abbreviations: ALP, alkaline phosphatase; AST, aspartate aminotransferase; COL1A1, collagen, type I, alpha 1; RUNX2, Runt-related transcription factor 2; PPARγ, peroxisome proliferator-activated receptor gamma; FBS, fetal bovine serum; CPC, cetylpyridinium chloride; BSA, bovine serum albumin; CTX-1, type I collagen C-terminal telopeptide; P1NP: pro-peptide of type I procollagen; BV/TV, bone volume fraction; Tb.N, trabecular number; Tb.Th, trabecular thickness; Tb.Sp, trabecular separation

Key words: indole-3-propionic acid, gut microbiota, bone-fat balance, PPARγ signalling pathway

Introduction

Osteoporosis (OP) is a prevalent metabolic bone disorder characterised by reduced bone mass and increased fracture susceptibility (1,2). With the aging global population, it poses a significant public health burden worldwide (3,4). Beyond bone loss itself, accumulating evidence suggests that OP fundamentally arises from dysregulated cellular dynamics within the bone marrow niche (5). Particularly, an imbalance in bone marrow stromal cell (BMSC) differentiation favouring adipogenesis over osteogenesis has emerged as a central pathological feature of the disease (6,7). In addition, inflammatory cytokines, including interleukin-1β (IL-1β), interleukin-6 (IL-6) and tumour necrosis factor-α, are well recognised to regulate bone remodelling by promoting osteoclast differentiation and activity while inhibiting osteoblast function (8,9), thereby contributing to enhanced bone resorption and bone loss. These cytokines also participate in extracellular matrix degradation through upregulation of proteolytic enzymes such as matrix metalloproteinases and cathepsin K, which are key mediators of bone matrix degradation in OP (10,11).

Under physiological conditions, BMSCs maintain skeletal integrity through tightly coordinated lineage commitment. However, oestrogen deficiency, aging and chronic oxidative stress disrupt this equilibrium, resulting in excessive accumulation of marrow adipocytes and impaired osteoblast formation (12). Reactive oxygen species not only induce

apoptosis of osteoprogenitor cells but also promote adipogenic differentiation, thereby exacerbating bone loss (13). Among the key molecular regulators governing this process, peroxisome proliferator-activated receptor gamma (PPARγ) serves as a master transcription factor that drives adipogenesis while simultaneously suppressing osteoblast differentiation (14,15). Aberrant activation of PPARγ has been consistently associated with osteoporotic phenotypes, highlighting it as a critical therapeutic target for restoring bone-fat balance (16-18).

In parallel with these intrinsic regulatory mechanisms, the gut microbiota has emerged as an important extrinsic modulator of skeletal homeostasis through the gut-bone axis (19,20). Microbial metabolites, particularly those derived from tryptophan metabolism, have attracted increasing attention because of their systemic regulatory functions (21), including the modulation of immune responses, oxidative stress and tissue homeostasis (22-24). Tryptophan can be metabolised by intestinal microbes into indole and its derivatives, including indole-3-acetic acid (IAA), indole-3-propionic acid (IPA), indole-3-acrylic acid (IA), indole-3-lactic acid (ILA) and indole-3-aldehyde (25). Among these metabolites, IPA, which is predominantly produced by *Clostridium sporogenes* (*C. sporogenes*) (26), has been reported to exert potent antioxidative (27,28), anti-inflammatory (29) and cytoprotective effects (30) in multiple disease contexts (31). Recent studies have suggested that IPA and related indole derivatives may influence bone metabolism (32-34), primarily through inhibition of osteoclastogenesis (35,36) and improvement of gut barrier function (36). For example, IPA was reported to improve skeletal quality by suppressing P65/NLRP3-dependent osteoclast formation in diet-induced obese mice (32). However, whether IPA directly regulates BMSC lineage commitment and contributes to the restoration of osteogenic-adipogenic balance remains largely unknown.

In the present study, it was demonstrated that microbiota-derived IPA acts as a critical regulator of bone marrow lineage fate by suppressing PPARγ signalling. Through integrated *in vitro* and *in vivo* analyses, it was revealed that IPA restores bone-fat balance, enhances osteogenesis, and alleviates oestrogen deficiency-induced OP. These findings reveal a previously unrecognised mechanism linking gut microbial metabolism to skeletal remodelling and highlight IPA as a promising therapeutic candidate for OP.

Materials and methods

Reagents and antibodies. IPA (cat. no. SJ-MX4391) was purchased from Shandong Sparkjade Scientific Instruments Co., Ltd. H_2O_2 was purchased from MilliporeSigma. Anti-GAPDH antibody was obtained from Cell Signalling Technology, Inc. Antibodies against COL1A1 (cat. no. HA722517), RUNX2 (cat. no. ET1612-47), SP7 (cat. no. HA722817) and OPN (cat. no. HA723082) were obtained from HUABIO. Anti-PPARγ antibody (cat. no. 14N93N79) was purchased from Epizyme, Inc.

Mouse BMSC isolation, culture and osteogenic differentiation. Mouse BMSCs (mBMSCs) were isolated as previously described (37,38). Briefly, mBMSCs were obtained from the femora and tibiae of C57BL/6 mice by flushing the bone marrow cavity. The C57BL/6 mice were sourced from same mice used in the animal experiments. The isolated cells were cultured in α-MEM (Procell Life Science & Technology Co., Ltd.) supplemented with 10% fetal bovine serum (FBS; cat. no. SA101.02; Cellmax; https://www.cellmaxcell.com/) and 1% penicillin/streptomycin (MedChemExpress). To establish an oxidative stress microenvironment *in vitro*, cells were treated with H_2O_2 (100 μM) for 2 h (7). For osteogenic differentiation, mBMSCs were cultured in osteogenic induction medium consisting of low-glucose Dulbecco's Modified Eagle Medium (Procell Life Science & Technology Co., Ltd.) supplemented with 10% FBS, β-glycerophosphate (10 mM), ascorbic acid (200 μM) and dexamethasone (100 nM) (MedChemExpress).

Alkaline phosphatase (ALP) and alizarin Red S (ARS) staining. mBMSCs were seeded in 24-well plates and cultured in osteogenic induction medium. At the indicated time points, ALP staining was performed using a BCIP/NBT Alkaline Phosphatase Chromogenic kit (cat. no. C3206; Beyotime Institute of Biotechnology) according to the manufacturer's instructions. ARS staining was performed using an Alizarin Red kit (cat. no. ALIR-10001; Cyagen Biosciences, Inc.) following the manufacturer's protocol.

Oil Red O staining. mBMSCs were seeded in 24-well plates and cultured in adipogenic induction medium ((Procell Life Science & Technology Co., Ltd.) according to the manufacturer's instructions. Cells were subsequently stained with Oil Red O staining solution (Procell Life Science & Technology Co., Ltd.).

Cell Counting Kit-8 (CCK-8) assay. To evaluate the effect of IPA on cell proliferation, 2,000 cells were seeded into 96-well plates and treated with different concentrations of IPA (0, 10, 25, 50, 75 and 100 μM) for the indicated durations. Subsequently, 10 μl of CCK-8 solution (Beijing Boxbio Science & Technology Co., Ltd.) was added to each well and incubated at 37˚C for 2 h. Absorbance at 450 nm was measured using a microplate reader (BioTek; Agilent Technologies, Inc.).

Mitochondrial membrane potential (MMP) assay. MMP was assessed using a JC-1 assay kit (MedChemExpress). Briefly, cells were pretreated with H_2O_2 (100 μM) and subsequently exposed to different concentrations of IPA for 12, 24, or 48 h. After treatment, cells were incubated with JC-1 working solution for 20 min. Fluorescence intensities were measured at 590 nm (aggregates, red) and 520 nm (monomers, green). The ratio of red-to-green fluorescence was calculated to evaluate changes in MMP.

Western blotting. Cells were harvested and lysed in RIPA buffer containing protease and phosphatase inhibitors (Beijing LABLEAD Inc.). Lysates were centrifuged at 12,000 x g for 15 min at 4˚C, and the supernatants were collected and mixed with loading buffer. Total protein concentration was determined using a BCA protein assay kit (cat. no. P0012; Beyotime Institute of Biotechnology). Equal amounts of protein (20 μg per lane) were separated by 10% sodium dodecyl sulphate polyacrylamide gel electrophoresis and transferred onto

Table I. Sequences of primers used for reverse transcription-quantitative PCR.

Gene name	Primer sequence (5'-3')
Col1a1	F: GCCGCAAAGAGTCTACATGT
	R: CTTCTTGGCCATGCGTCAG
Runx2	F: CACCTCGAATGGCAGCACGCTA
	R: GCCGCCAAACAGACTCATCCA
Sp7	F: CCTAAGGGGCACAGCTCGTCT
	R: TGCATGTCCCACCAAGGAGTAGG
Ocn	F: CAGTATGGCTTGAAGACCGC
	R: GACATCCATACTTGCAGGGC
Adiponectin	F: CTGCAACATTCCGGGACTCT
	R: TGAAGAGAACGGCCTTGTCC
Srebp-1	F: ACAGGAGGACATCTTGCTGC
	R: AGATCTCTGCCAGTGTTGCC
CEBPα	F: GACATCAGCGCCTACATCGA
	R: CCCGGGTAGTCAAAGTCACC
Fabp2	F: GCCTGGACCATTGAGGGAAA
	R: GCTTGGCCTCAACTCCTTCA
PPARγ	F: AAGCCGTGCAAGAGATCACA
	R: TGGTCATGAATCCTTGGCCC
GAPDH	F: GGCAAATTCAACGGCACAGTCAAG
	R: TCGCTCCTGGAAGATGGTGATGG
*338F_806R	F: ACTCCTACGGGAGGCAGCAG
	R: GGACTACHVGGGTWTCTAAT

*H/V/W represent degenerate bases in the primer sequence, which are used to improve amplification coverage for different bacterial species. F, forward; R, reverse; COL1A1, collagen, type I, alpha 1; RUNX2, Runt-related transcription factor 2; PPARγ, peroxisome proliferator-activated receptor gamma; SREBP, sterol regulatory element-binding protein.

polyvinylidene fluoride membranes (MilliporeSigma). Membranes were blocked at room temperature with 5% non-fat milk for 1 h and incubated with primary antibodies (1:1,000) overnight at 4˚C. The membranes were then incubated with HRP-conjugated secondary antibodies (1:5,000) for 1 h. Protein bands were visualised using ECL Luminescent Solution (cat. no. KGC4601; Nanjing KeyGen Biotech Co., Ltd.) using a chemiluminescent detection system (Thermo Fisher Scientific, Inc.), and band intensities were analysed using the 'Gel Analysis' function in ImageJ software (V1.53; National Institutes of Health) as previously described (39). GAPDH was used as the internal loading control.

Reverse transcription-quantitative polymerase chain reaction (RT-qPCR). Total RNA from BMSCs was extracted using TRIzol reagent (Shandong Sparkjade Scientific Instruments Co., Ltd.), and cDNA was synthesised using the SPARKscript II RT Plus Kit (cat. no. AG0304; Shandong Sparkjade Scientific Instruments Co., Ltd.). RT-qPCR was performed using SYBR Green Master Mix (cat. no. AH0104; Shandong Sparkjade Scientific Instruments Co., Ltd.). Thermal cycling conditions were set according to the manufacturer's instructions. The mRNA levels of the target genes were normalized to those of the housekeeping gene GAPDH. The relative gene expression levels were calculated using the $2^{-\Delta\Delta Cq}$ method. Primer sequences used in the present study are listed in Table I.

Immunofluorescence (IF). For IF staining, mBMSCs were fixed with 4% paraformaldehyde and permeabilised with 0.1% Triton X-100 (Beyotime Institute of Biotechnology). Cells were then blocked with 5% bovine serum albumin (BSA; MilliporeSigma) and incubated at 4˚C with primary antibodies [PPARγ, COL1A1, RUNX2 (cat. no. K003506P) Beijing Solarbio Science & Technology Co., Ltd.] overnight. The following day, cells were incubated at room temperature with fluorophore-conjugated secondary antibodies. Nuclei were counterstained with DAPI with 5 μg/ml (Beyotime Institute of Biotechnology). Fluorescence signals were detected using a confocal microscope (Leica Microsystems GmbH) at x400 magnification. Fluorescence intensity was analysed using ImageJ software.

Molecular docking. The molecular docking analysis of IPA and PPARγ was performed using the CB-Dock2 platform (https://cadd.labshare.cn/cb-dock2/index.php), as previously described (40). The structure of IPA (PubChem compound ID: 3744) was obtained from PubChem (https://pubchem.ncbi.nlm.nih.gov/compound/3744), whereas the crystal structure of PPARγ (8BF1) was downloaded from the Protein Data Bank (https://www.rcsb.org/structure/8BF1). The binding sites and binding affinity between IPA and PPARγ were subsequently predicted.

RNA sequencing. Total RNA from BMSCs was extracted using TRIzol reagent according to the manufacturer's

instructions. RNA quality and integrity were assessed using 5300 Bioanalyser (Agilent Technologies, Inc.), and samples with RNA integrity number OD260/280=1.8~2.2 were used for library construction. Sequencing libraries were generated using the NEBNext Ultra II RNA Library Prep Kit (cat. no. E7770; New England Biolabs) according to the manufacturer's instructions. The final library concentration was determined using a Qubit fluorometer (Thermo Fisher Scientific, Inc.) and quantitative PCR, and libraries were loaded at a concentration of 4 nM for sequencing on the Illumina NovaSeq platform, yielding ~50 million paired-end reads per sample. Raw data processing, including adaptor trimming and quality filtering, was performed using FastQC (v. 0.11.9; https://www.bioinformatics.babraham.ac.uk/projects/fastqc/). High-quality reads were aligned to the mouse reference genome using HISAT2 (v. 2.2.1; https://daehwankimlab.github.io/hisat2/). Transcript abundance was quantified and expressed as transcripts per million. Gene Ontology (GO) and Kyoto Encyclopaedia of Genes and Genomes (KEGG) pathway enrichment analyses were performed using the Majorbio online analysis platform (https://www.majorbio.com/).

16S rRNA gene sequencing. Microbial DNA was extracted from faecal samples collected from sham and ovariectomy (OVX) mice. The 338F/806R primers (Table I) were used to amplify the V3-V4 region of the bacterial 16S rRNA gene, and PCR products were purified using a PCR Clean-Up Kit (YuHua Biotechnology). Sequencing libraries were prepared and sequenced according to the manufacturer's instructions to generate paired-end 300-bp reads. All sequencing and bioinformatics analyses were performed by Majorbio Bio-Pharm Technology.

IPA concentration measurement. Serum samples were collected from Sham and OVX mice. Serum IPA concentrations were measured using gas chromatography-mass spectrometry according to the manufacturer's instructions.

Animal experiments. All animal procedures were approved by Peking University Third Hospital (approval no. BCAA0292; Beijing, China) and conducted in accordance with ARRIVE guidelines. 8-week-old female C57BL/6 mice were acclimated for 1 week under standard laboratory conditions. The initial body weight of the mice was ~18-22 g at the start of the experiment. Animals were housed at 22±2˚C with 50±10% humidity under a 12 h light/dark cycle. Food and water were available ad libitum throughout the study. A total of 24 mice were randomly assigned to 4 groups: Sham, OVX, OVX + IPA (10 mg/kg) and OVX + IPA (20 mg/kg). A postmenopausal OP model was established by bilateral OVX as previously described (41). Briefly, the mice were anaesthetised via inhalation of 3% isoflurane, with the anaesthesia maintained via 2% isoflurane inhalation during surgery, and a small dorsal midline incision was made to expose both ovaries, which were subsequently ligated and removed. Sham-operated mice underwent the same surgical procedure without ovary removal. Following surgery, mice received daily oral administration of IPA or an equal volume of normal saline for 10 weeks. At the end of the experiment, animals were euthanized by overdose of pentobarbital sodium administered via intraperitoneal injection (150 mg/kg). Death was confirmed by the absence of spontaneous respiration, heartbeat and pedal withdrawal reflex. The femurs and serum samples were collected for further analyses. A total of ~600 μl of whole blood was collected via orbital blood sampling following eyeball removal, and serum was subsequently isolated by centrifugation at 3,000 x g for 15 min at 4˚C.

Micro-CT and histological analysis. Femurs were scanned using a SkyScan micro-CT system (Bruker Corporation). The region of interest was defined as a 1-mm-high area distal to the growth plate. Three-dimensional reconstruction images were generated using CTvox software. Trabecular bone parameters, including bone volume fraction (BV/TV), trabecular number (Tb.N), trabecular thickness (Tb.Th) and trabecular separation (Tb.Sp), were analysed using CTAn software (V2.0; https://www.blue-scientific.com/bruker-micro-ct-software/). For haematoxylin and eosin (H&E) staining, decalcified bone tissues were processed and stained according to the manufacturer's protocols (Wuhan Servicebio Technology Co., Ltd.).

Von Kossa staining. Undecalcified bone samples were subjected to Von Kossa staining according to the manufacturer's instructions (Wuhan Servicebio Technology Co., Ltd.). Images were captured using a light microscope, and mineralised areas were quantified using ImageJ software.

Immunohistochemistry (IHC). Decalcified bone tissues were embedded in paraffin. Tissue sections (5 μm) were deparaffinised in xylene and rehydrated through a graded ethanol series (100, 95, 85, and 75% ethanol) before antigen retrieval by trypsin digestion. Sections were then blocked with 3% hydrogen peroxide and incubated with 5% BSA for 1 h. Subsequently, the sections were incubated at 4˚C with primary antibodies overnight. The following day, HRP-conjugated secondary antibodies were applied at room temperature for 1 h. Signals were developed using a DAB substrate. Images were acquired under a bright-field microscope, and staining intensity was quantified using ImageJ software.

Enzyme-linked immunosorbent assay. Serum levels of P1NP and CTX-1 were measured using ELISA kits (cat. nos. E-EL-M3023 and E-EL-M0233; Elabscience Biotechnology, Inc.) according to according to the manufacturer. Absorbance at 450 nm was measured using a microplate reader (BioTek; Agilent Technologies, Inc.). All samples were analysed in triplicate.

Statistical analysis. Data were presented as the mean ± SD. All experiments were independently repeated at least three times. Comparisons between two groups were performed using unpaired Student's t-test, whereas comparisons among multiple groups were analysed using one-way or two-way analysis of variance followed by Tukey's post hoc test. $P<0.05$ was considered to indicate a statistically significant difference. Statistical analyses and data visualisation were performed using GraphPad Prism (v. 8.0; Dotmatics).

Results

C. sporogenes-derived IPA is depleted in OP *and correlates with bone loss*. To investigate whether gut microbiota-derived metabolites contribute to OP, an OVX-induced mouse model was first established. The OVX model effectively mimicked postmenopausal OP (42). Micro-CT analysis confirmed a marked reduction in trabecular bone mass in OVX mice, validating the successful establishment of osteoporotic phenotypes (Fig. 1A and B). 16S rRNA sequencing was next performed to profile gut microbiota composition. Although α-diversity did not differ significantly between groups (Fig. 1C), β-diversity analysis revealed a clear separation between sham and OVX mice, indicating substantial alterations in microbial community structure (Fig. 1D). Consistently, the gut microbial health index was significantly reduced in the OVX group (Fig. S1A), whereas the microbial dysbiosis index was significantly increased (Fig. S1B).

Taxonomic profiling identified distinct alterations in bacterial genera between the two groups. OVX mice exhibited increased abundance of *Muribaculaceae* and reduced abundance of the *Lactobacillus* and *Clostridia* genera compared with sham controls (Fig. 1E). The abundance of *Clostridia* was significantly decreased in the OVX group, with statistical significance confirmed by Wilcoxon analysis (Fig. 1F and G). Given that *Clostridia* is a major bacterial genus involved in IPA production (26), serum IPA concentrations were next measured. Metabolite analysis demonstrated a significant reduction in circulating IPA levels in OVX mice (Fig. 1H). Importantly, correlation analyses revealed that serum IPA levels were positively associated with both BV/TV and *Clostridium* abundance (Fig. 1I and J). These findings suggested that depletion of microbiota-derived IPA is a characteristic feature of oestrogen deficiency-induced OP and may contribute functionally to bone loss.

IPA protects BMSCs against oxidative stress-induced apoptosis. It was next investigated whether IPA modulates BMSC survival under oxidative stress conditions. CCK-8 assays demonstrated that IPA alone (0-100 μM) neither promoted nor inhibited mBMSC proliferation (Fig. 2A). Exposure to H_2O_2 significantly reduced cell viability, whereas IPA treatment dose-dependently rescued this effect without altering basal proliferation (Fig. 2B). Live/dead staining further confirmed that IPA markedly attenuated oxidative stress-induced cell death (Fig. 2C and D).

Because loss of MMP is a hallmark of early apoptosis (43), JC-1 staining was performed to evaluate mitochondrial function. H_2O_2 treatment induced a significant reduction in MMP, whereas IPA administration effectively restored mitochondrial integrity (Fig. 2E and F). Collectively, these results demonstrated that IPA exerts cytoprotective effects on BMSCs by preserving mitochondrial function and attenuating oxidative stress-induced apoptosis.

IPA restores osteogenic capacity and suppresses adipogenic differentiation under oxidative stress. It was next examined whether IPA directly regulates BMSC lineage commitment. Under physiological conditions, IPA did not significantly affect mineralised nodule formation (Fig. S2A and B) or ALP activity (Fig. S2C and D). Consistently, western blot analysis showed that IPA had no appreciable effect on the expression of osteogenic markers, including RUNX2, SP7, and OPN (Fig. S2E and F). These findings indicate that IPA does not function as a basal osteo-inductive factor.

By contrast, under oxidative stress conditions, H_2O_2 markedly impaired osteogenic differentiation, as evidenced by reduced ALP activity and decreased mineralised nodule formation (Fig. 3A and B). IPA treatment dose-dependently restored osteogenic capacity (Fig. 3D and E). In parallel, oxidative stress significantly promoted adipogenic differentiation (42), as reflected by increased lipid accumulation and upregulation of adipogenic markers (Fig. 3C and F). Further analysis of lineage-specific gene expression demonstrated that IPA prevented the H_2O_2-induced downregulation of osteogenic genes, including Col1a1, Runx2, Sp7 and Ocn (Fig. S3A), while reversing the upregulation of adipogenic genes, including *Adiponectin*, Cebpα, Fabp2 and Srebp-1 (Fig. S3B). Western blot analysis further confirmed that IPA rescued the H_2O_2-induced downregulation of osteogenic proteins (Fig. 3G and H). Similar findings were observed by IF staining (Fig. 3I; Fig. S4A and B), further supporting the protective effect of IPA on osteogenic differentiation under oxidative stress conditions. Together, these findings indicated that IPA functions as a context-dependent regulator that restores osteogenic-adipogenic balance under pathological conditions rather than altering baseline differentiation.

IPA supplementation alleviates bone loss and enhances bone formation in vivo. To determine whether these protective effects also occur *in vivo*, an OVX mouse model was established and IPA was administered orally for 10 weeks. A schematic overview of the animal experimental design is presented in Fig. 4A. OVX mice exhibited significantly increased body weight and reduced uterine weight compared with the control group (Fig. S5A and B).

Micro-CT analysis revealed that IPA markedly alleviated OVX-induced bone loss (Fig. 4B). IPA supplementation significantly improved trabecular bone architecture, as indicated by increased BV/TV, Tb.N and Tb.Th, along with reduced Tb.Sp (Fig. 4E-H). Consistently, biochemical analyses demonstrated elevated levels of the bone formation marker PINP and decreased levels of the bone resorption marker CTX-1 following IPA treatment, indicating a shift toward anabolic bone remodelling (Fig. 4C and D). These results demonstrated that IPA supplementation effectively mitigates oestrogen deficiency-induced bone loss and promotes bone formation *in vivo*.

IPA corrects the osteogenic-adipogenic imbalance in the bone marrow of OVX mice. To investigate further the cellular basis of these effects, BMSCs isolated from experimental mice were analysed. Cells derived from OVX mice exhibited impaired mineralisation capacity, as reflected by significantly reduced ALP activity and ARS staining ability (Fig. 5A and B), along with increased intracellular lipid accumulation, confirming disruption of lineage balance (Fig. 5H). Importantly, IPA treatment restored osteogenic capacity (Fig. 5C and D) while

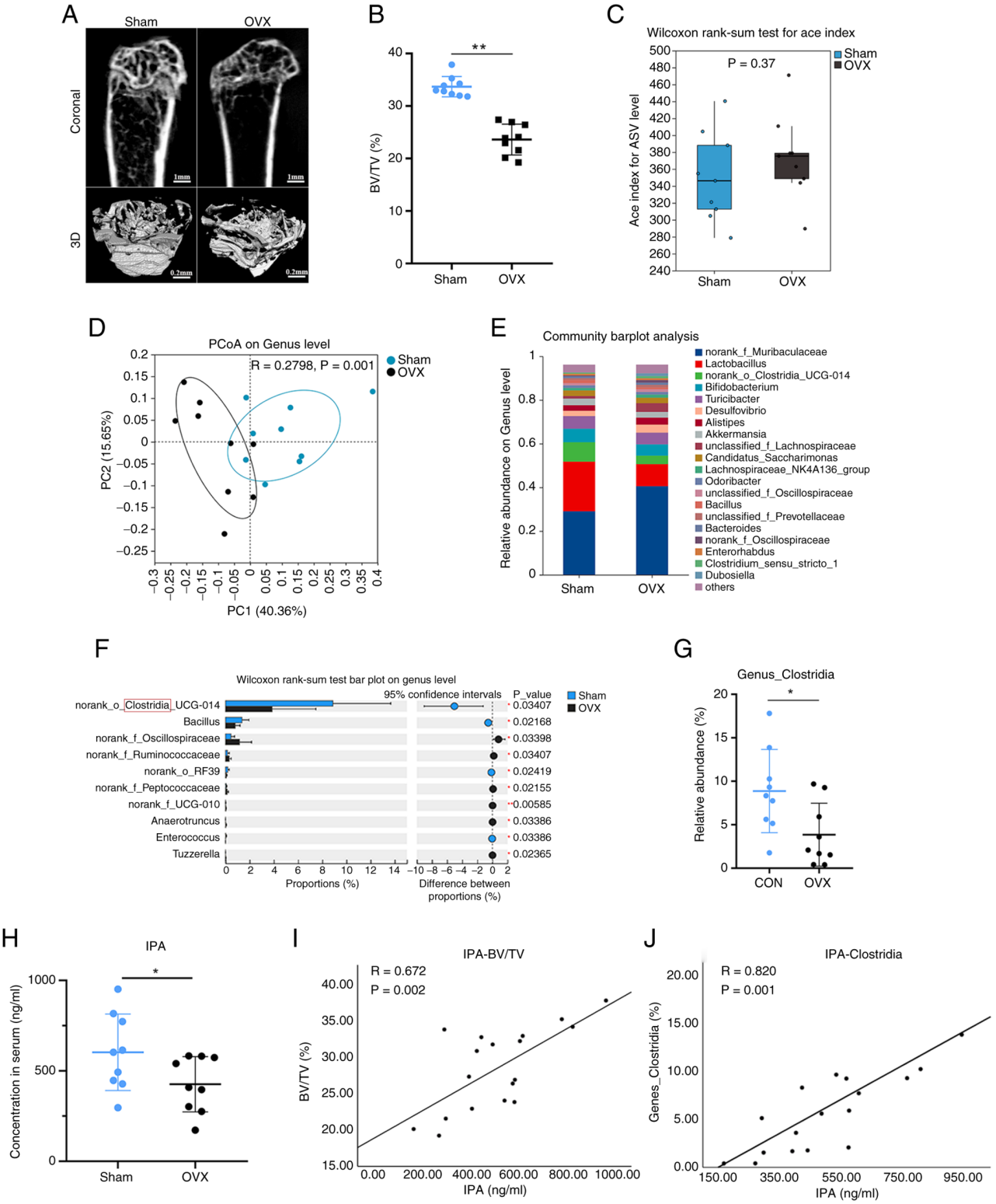

Figure 1. Decreased *C. sporogenes* abundance and reduced IPA levels in OVX-induced osteoporotic mice. (A) Representative micro-CT images of Sham and OVX mice (n=9). (B) Quantification of BV/TV between the two groups. (C) α-diversity analysis based on the ACE index. (D) β-diversity analysis based on principal coordinate analysis. (E) Relative abundance of gut microbiota at the genus level (n=9). (F) Wilcoxon rank-sum test analysis of gut microbiota at the genus level between the two groups. (G) Relative abundance of the *Clostridia* genus between the two groups. (H) Serum IPA concentrations in the two groups. (I) Spearman correlation analysis between IPA levels and BV/TV. (J) Spearman correlation analysis between IPA levels and the *Clostridia* genus. Data are presented as the mean ± SD. *P<0.05 and **P<0.01 compared with the control group. IPA, indole-3-propionic acid; OVX, ovariectomy; BV/TV, bone volume fraction.

suppressing adipogenesis (Fig. 5I) in BMSCs isolated from OVX mice. IPA administration significantly upregulated the expression of osteogenic genes and proteins (Fig. 5E-G), while suppressing adipogenic gene expression in OVX mice (Fig. 5J). These findings demonstrated that IPA alleviates OP by re-establishing bone marrow lineage equilibrium.

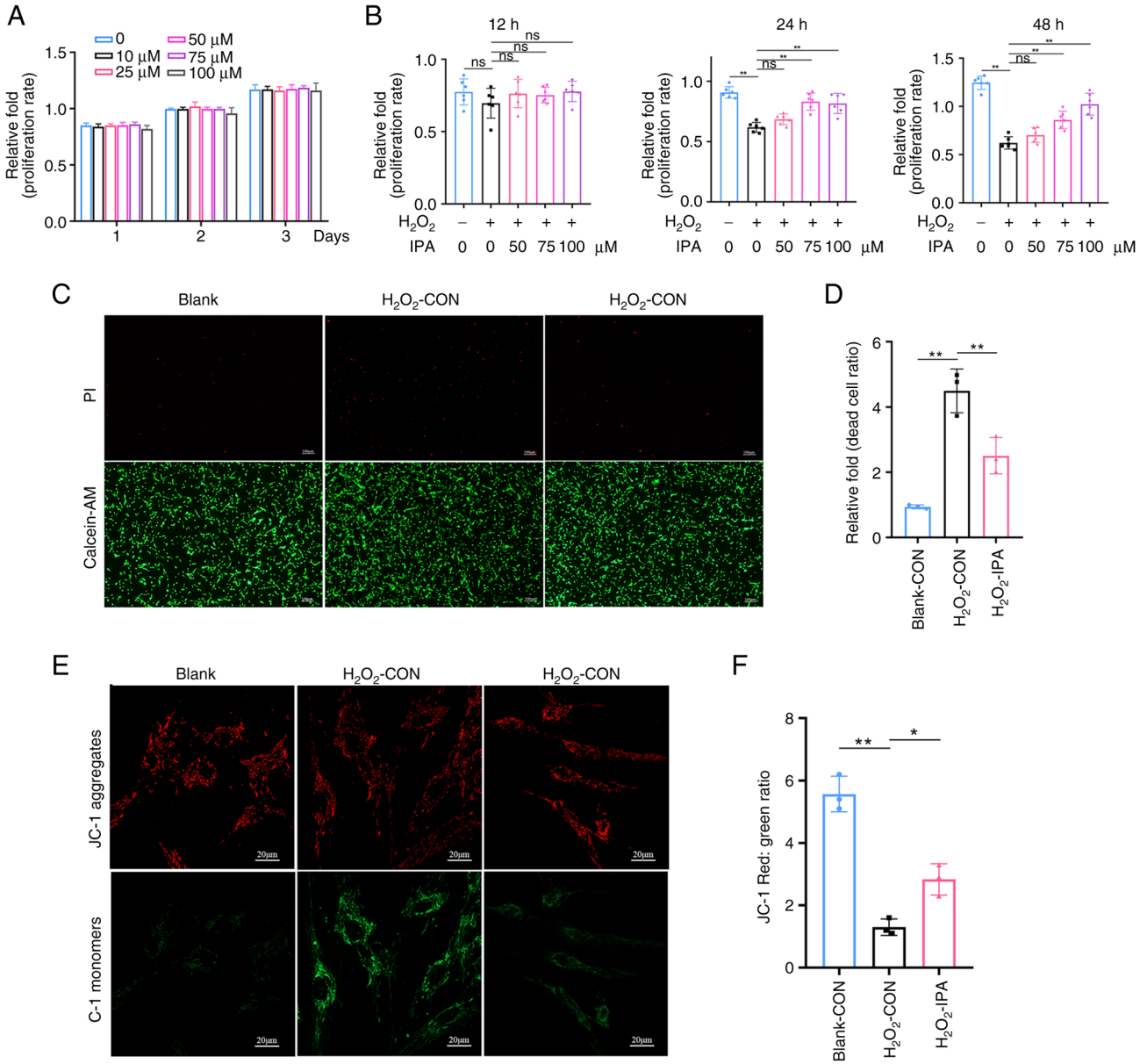

Figure 2. IPA protects mBMSCs against H_2O_2-induced apoptotic injury. (A) Effects of IPA on mBMSC viability over 1, 2, and 3 days, as determined by the CCK-8 assay. (B) Effects of IPA pretreatment on mBMSC viability following H_2O_2 exposure for 12, 24, and 48 h, as determined by the CCK-8 assay. (C) Live/dead staining of mBMSCs on day 1 using propidium iodide (dead cells) and Calcein-AM (live cells). (D) Quantification of the dead-cell ratio based on live/dead staining. (E) Mitochondrial membrane potential of H_2O_2-treated mBMSCs with or without IPA treatment for 1 day, assessed by JC-1 staining. (F) Quantification of the red/green fluorescence ratio from JC-1 staining. All experiments were repeated at least three times. Data are presented as the mean ± SD. **P<0.01 compared with the control group. IPA, indole-3-propionic acid; mBMSCs, mouse bone marrow stromal cells; CCK-8, Cell Counting Kit-8; ns, not significant.

IPA reprograms BMSC fate through suppression of PPARγ signalling. To elucidate the underlying mechanisms, transcriptomic sequencing was performed on mBMSCs treated with H_2O_2 in the presence or absence of IPA. RNA-seq analysis identified a total of 1,254 differentially expressed genes (DEGs; fold change ≥3.0), including 509 upregulated and 745 downregulated genes (Figs. 6A and S6A). GO functional annotation revealed that IPA-regulated genes were enriched in pathways associated with oxidative stress defence, cell proliferation and immune regulation (Fig. S6B). GO enrichment analysis further highlighted biological processes related to osteogenic differentiation, cell cycle regulation and oxidative phosphorylation (Fig. 6B). KEGG pathway analysis demonstrated significant enrichment in PPAR signalling, cholesterol biosynthesis, adipogenesis-related pathways, oxidative phosphorylation, and p53-mediated apoptosis (Fig. 6C). Gene Set Enrichment Analysis further showed that IPA markedly suppressed several adipogenesis-related pathways, including unsaturated fatty acid synthesis, cholesterol biosynthesis, and the PPARγ signalling pathway, while also inhibiting oxidative phosphorylation (Fig. 6D). These findings suggested that IPA preserves osteogenic function under oxidative stress, at least in part, by inhibiting adipogenic differentiation.

The three-dimensional structure of IPA is shown in Fig. 6E. Molecular docking analysis revealed a high

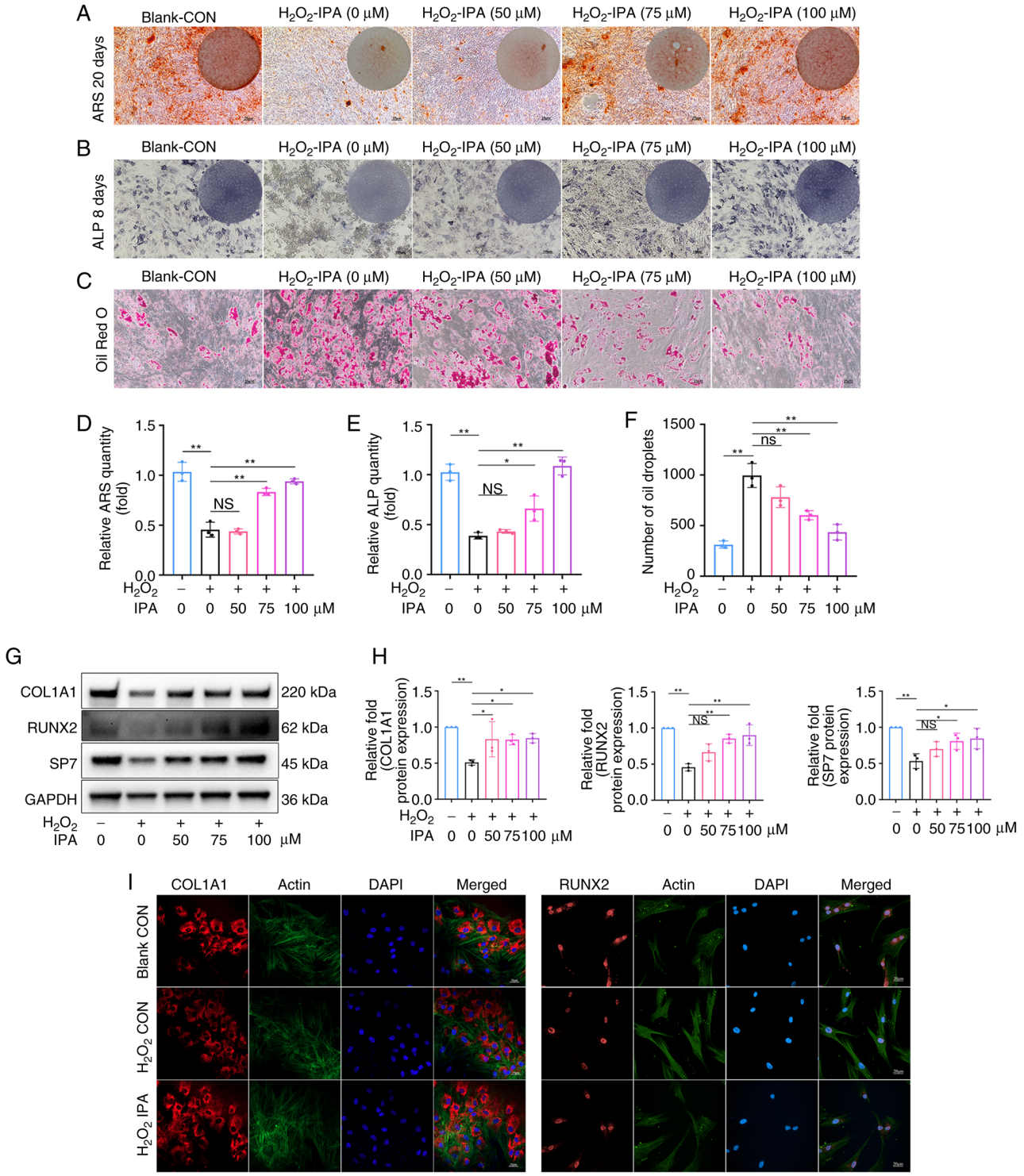

Figure 3. IPA attenuates H_2O_2-induced suppression of osteogenic function *in vitro*. (A) ARS staining of mBMSCs after 20 days of osteogenic differentiation. Scale bar, 25 μm. (B) ALP staining of mBMSCs after 8 days of osteogenic differentiation. Scale bar, 100 μm. (C) Oil Red O staining of mBMSCs after 8 days of osteogenic differentiation. Scale bar, 25 μm. (D) Quantification of ARS staining. (E) Quantification of ALP staining. (F) Quantification of Oil Red O staining. (G) Expression of osteogenesis-related proteins in mBMSCs after 5 days of osteogenic differentiation, assessed by western blotting. (H) Quantification of western blot results. (I) Representative immunofluorescence images of *RUNX2* and *COL1A1* expression. Scale bar, 20 μm. All experiments were repeated at least three times. Data are presented as the mean ± SD. *P<0.05 and **P<0.01 compared with the control group. IPA, indole-3-propionic acid; ARS, alizarin Red S; mBMSCs, mouse bone marrow stromal cells; ALP, alkaline phosphatase; COL1A1, collagen, type I, alpha 1; RUNX2, Runt-related transcription factor 2; NS, not significant.

predicted binding affinity (-6.6 kcal/mol) between IPA and PPARγ (Fig. 6F and G). Docking results demonstrated that IPA formed multiple hydrogen bonds and ionic interactions with key residues, including Arg280, Ile262 and Ile281, indicating a plausible structural basis for direct interaction (Fig. 6H). Consistently, H_2O_2-induced upregulation of PPARγ expression was significantly attenuated by IPA at both the mRNA and protein levels (Fig. 6I-K).

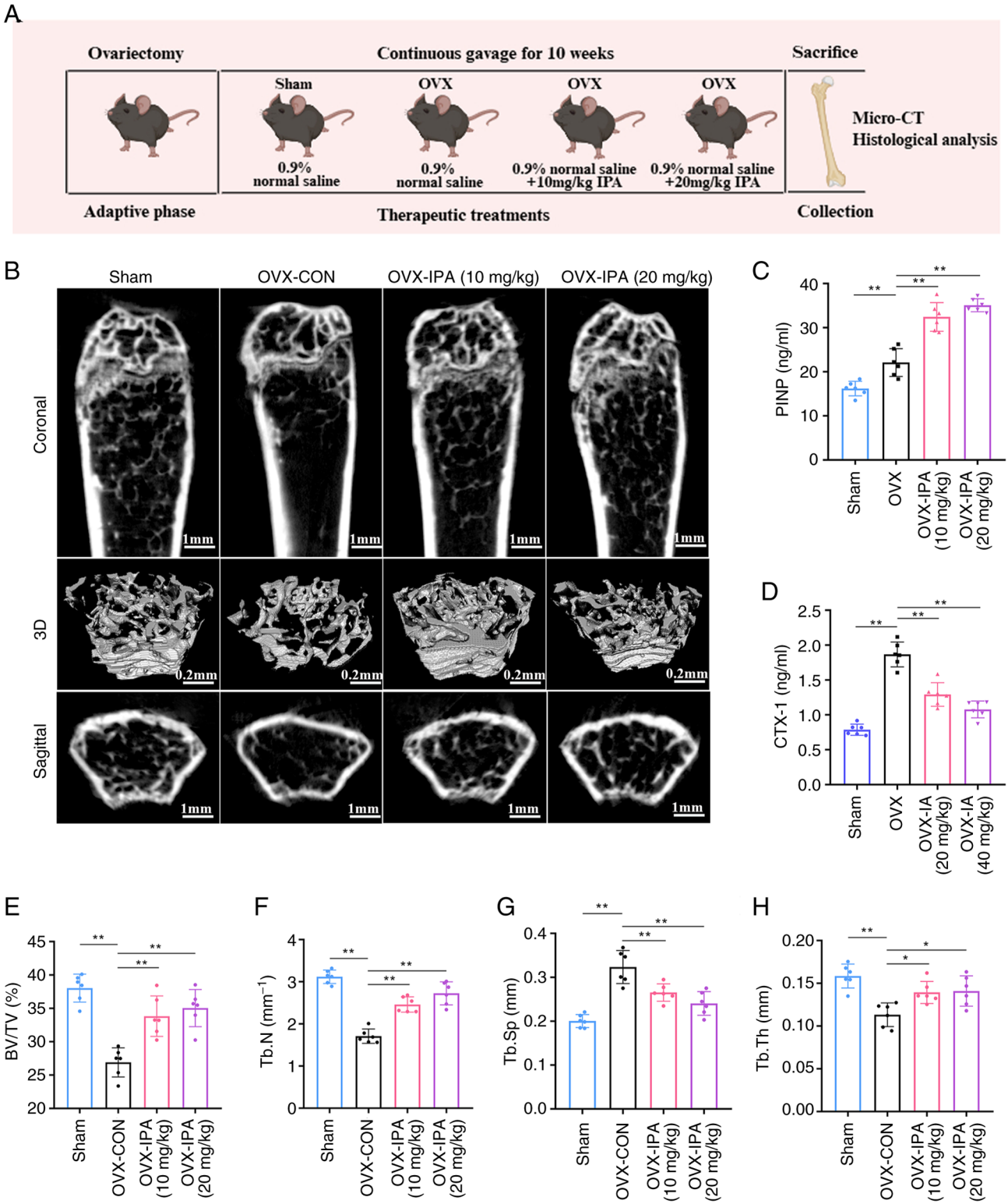

Figure 4. IPA supplementation mitigates OVX-induced bone loss and enhances bone formation. (A) Schematic overview of the animal experimental workflow. (B) Representative micro-CT images of distal femurs from the four experimental groups (n=6). (C) Serum concentrations of PINP. (D) Serum concentrations of CTX-1. (E-H) Quantification of trabecular bone parameters, including BV/TV, Tb.N, Tb.Sp and Tb.Th. Data are presented as the mean ± SD. *P<0.05 and **P<0.01 compared with the control group. IPA, indole-3-propionic acid; OVX, ovariectomy; BV/TV, bone volume fraction; Tb.N, trabecular number; Tb.Th, trabecular thickness; Tb.Sp, trabecular separation

IF analysis further confirmed reduced nuclear localisation of PPARγ following IPA treatment (Fig. 6L and N). Consistent with the *in vitro* findings, BMSCs isolated from OVX mice displayed elevated PPARγ expression, which was significantly reduced following IPA supplementation *in vivo* (Fig. 6M and O). These findings indicated that IPA regulates BMSC lineage commitment by inhibiting PPARγ signalling.

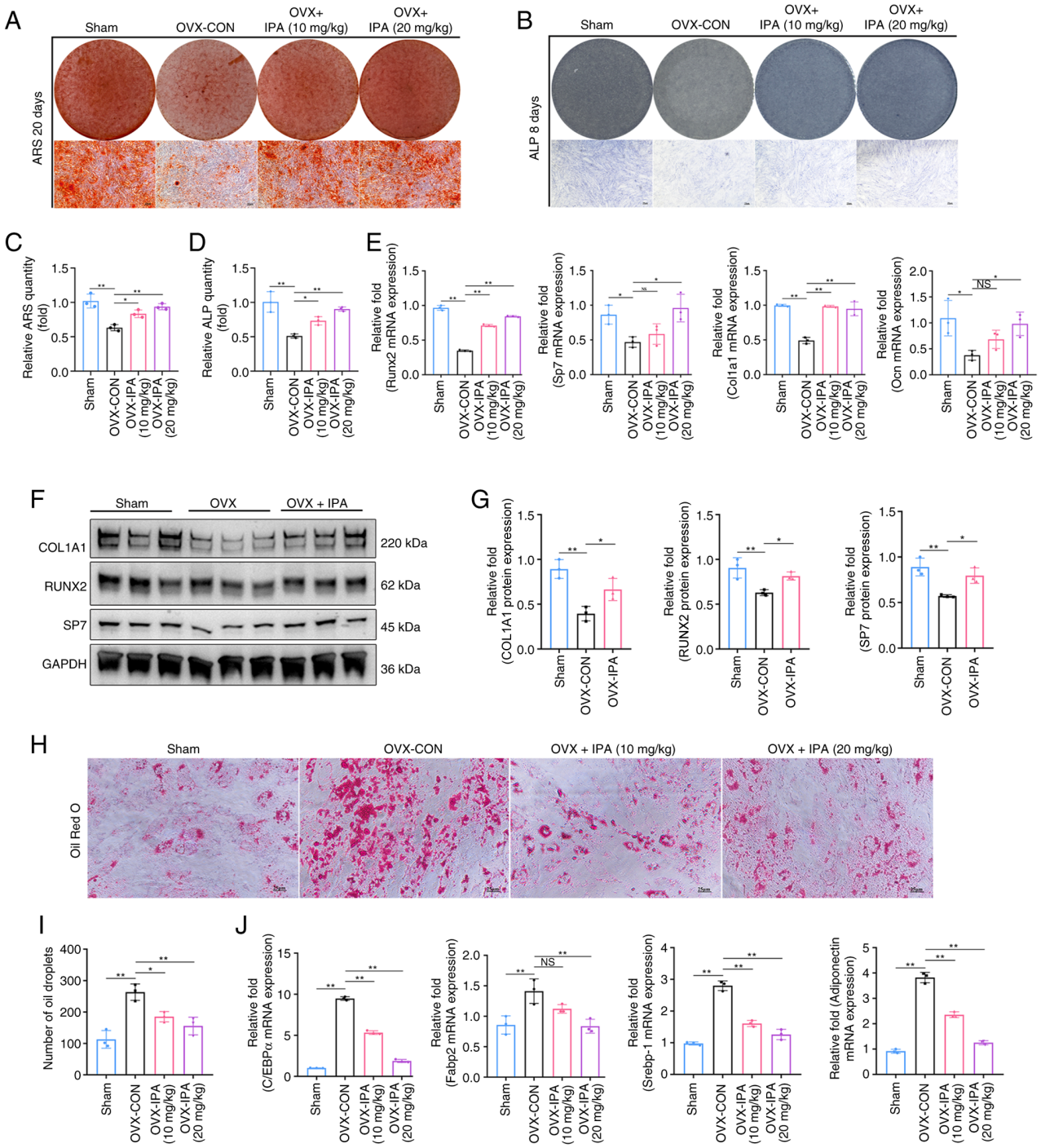

Figure 5. IPA restores OVX-induced bone-fat imbalance *in vivo*. (A) ARS staining of mBMSCs isolated from mice after 20 days of osteogenic differentiation. Scale bar, 25 μm. (B) ALP staining of mBMSCs isolated from mice after 8 days of osteogenic differentiation. Scale bar, 25 μm. (C) Quantification of ARS staining. (D) Quantification of ALP staining. (E) Expression of osteogenesis-related genes after 7 days of osteogenic differentiation, assessed by RT-qPCR. (F) Expression of osteogenic-related proteins after 7 days of osteogenic differentiation examined using western blot analysis. (G) Quantification of results of western blot analysis. (H) Oil Red O staining of mBMSCs isolated from mice after 8 days of adipogenic differentiation. Scale bar, 25 μm. (I) Quantification of Oil Red O staining. (J) Expression of adipogenesis-related genes after 10 days of adipogenic differentiation, assessed by RT-qPCR. All experiments were repeated at least 3 times. Data are presented as the mean ± SD. *P<0.05 and **P<0.01 compared with the control group. IPA, indole-3-propionic acid; OVX, ovariectomy; ARS, alizarin Red S; mBMSCs, mouse bone marrow stromal cells; ALP, alkaline phosphatase; RT-qPCR, reverse transcription-quantitative PCR; NS, not significant.

IPA supplementation suppresses PPARγ signalling to promote bone formation in vivo. To validate this mechanism *in vivo*, histological and IHC analyses were performed. H&E staining revealed that IPA supplementation significantly improved BV/TV compared with the OVX group (Fig. 7A). Consistent with the H&E staining results, Von Kossa staining demonstrated reduced mineral deposition in OVX mice, which was effectively restored following IPA administration (Fig. 7B). IHC analysis further confirmed these observations. BMSCs derived from OVX-induced osteoporotic mice exhibited lower expression of osteogenic proteins, including COL1A1 and RUNX2, whereas IPA treatment restored their expression levels (Fig. 7C and D). By contrast, PPARγ expression was significantly downregulated by IPA supplementation

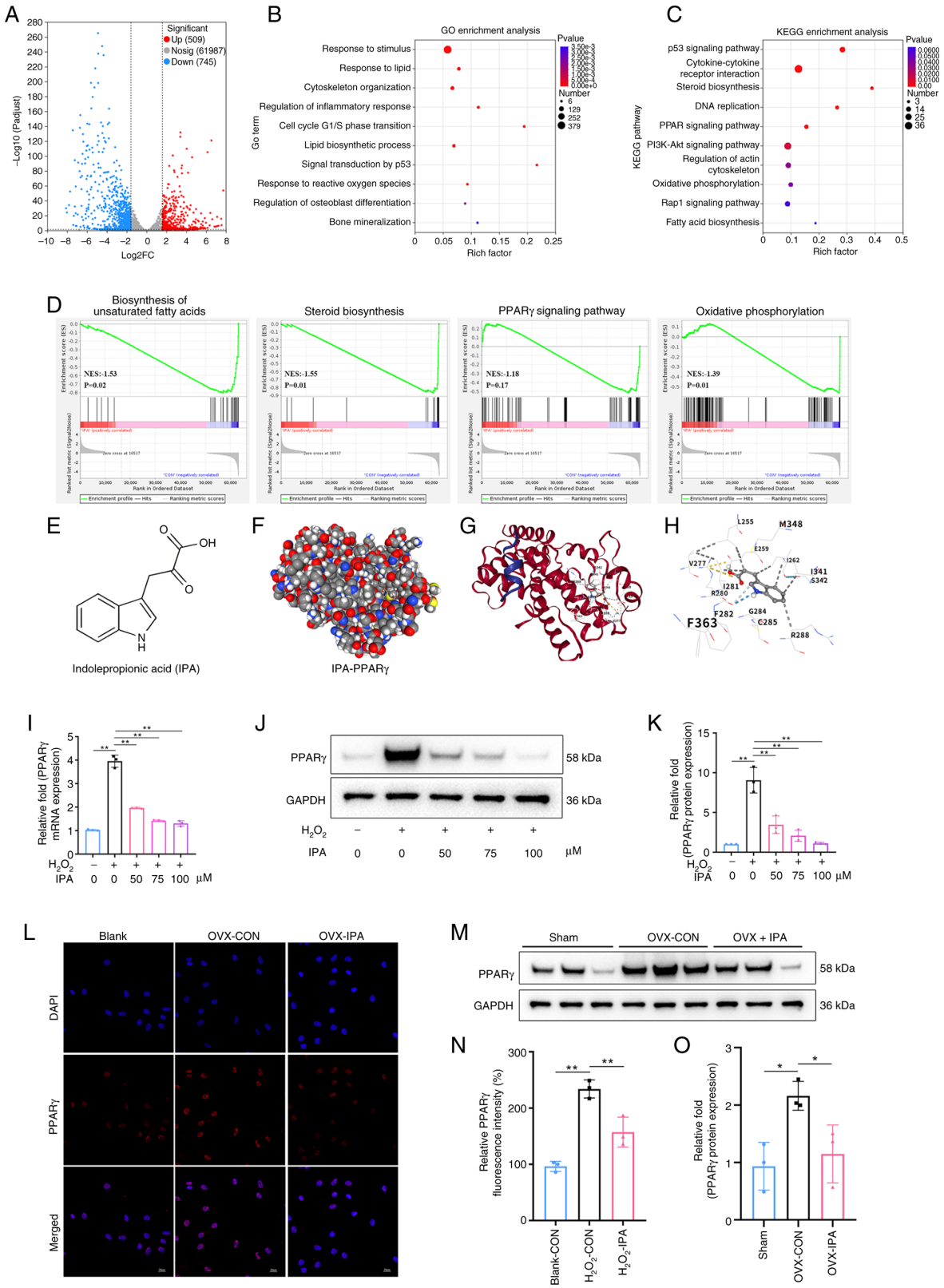

Figure 6. IPA regulates the osteogenic-adipogenic balance of BMSCs by targeting the PPARγ signalling pathway. (A) Volcano plots of DEGs between the two groups (n=3 per group). (B) GO biological process enrichment analysis of common DEGs. (C) KEGG enrichment analysis showing significantly altered signalling pathways following IPA treatment. (D) Gene Set Enrichment Analysis of pathways related to biosynthesis of unsaturated fatty acids, steroid biosynthesis, the PPARγ signalling pathway and oxidative phosphorylation. (E) Chemical structure of IPA. (F) Three-dimensional docking model of IPA and PPARγ. (G) Two-dimensional docking model of IPA and PPARγ. (H) Specific binding sites between AKT and including indole-3-acetic acid. (I) Expression of PPARγ mRNA assessed by reverse transcription-quantitative PCR. (J) Expression of PPARγ protein assessed by western blotting. (K) Quantification of western blot results. (L) Representative IF images of PPARγ expression in the presence of IPA (100 μM). Scale bar, 20 μm. (M) Expression of PPARγ protein in mBMSCs isolated from mice *in vivo*, assessed by western blotting. (N) Quantification of PPARγ fluorescence intensity by IF analysis. (O) Quantification of western blot results. All experiments were repeated at least three times. Data are presented as the mean ± SD. *P<0.05 and **P<0.01 compared with the control group. IPA, indole-3-propionic acid; BMSCs, bone marrow stromal cells; PPARγ, peroxisome proliferator-activated receptor gamma; DEGs, differentially expressed genes; GO, Gene Ontology; KEGG, Kyoto Encyclopedia of Genes and Genomes; IF, immunofluorescence.

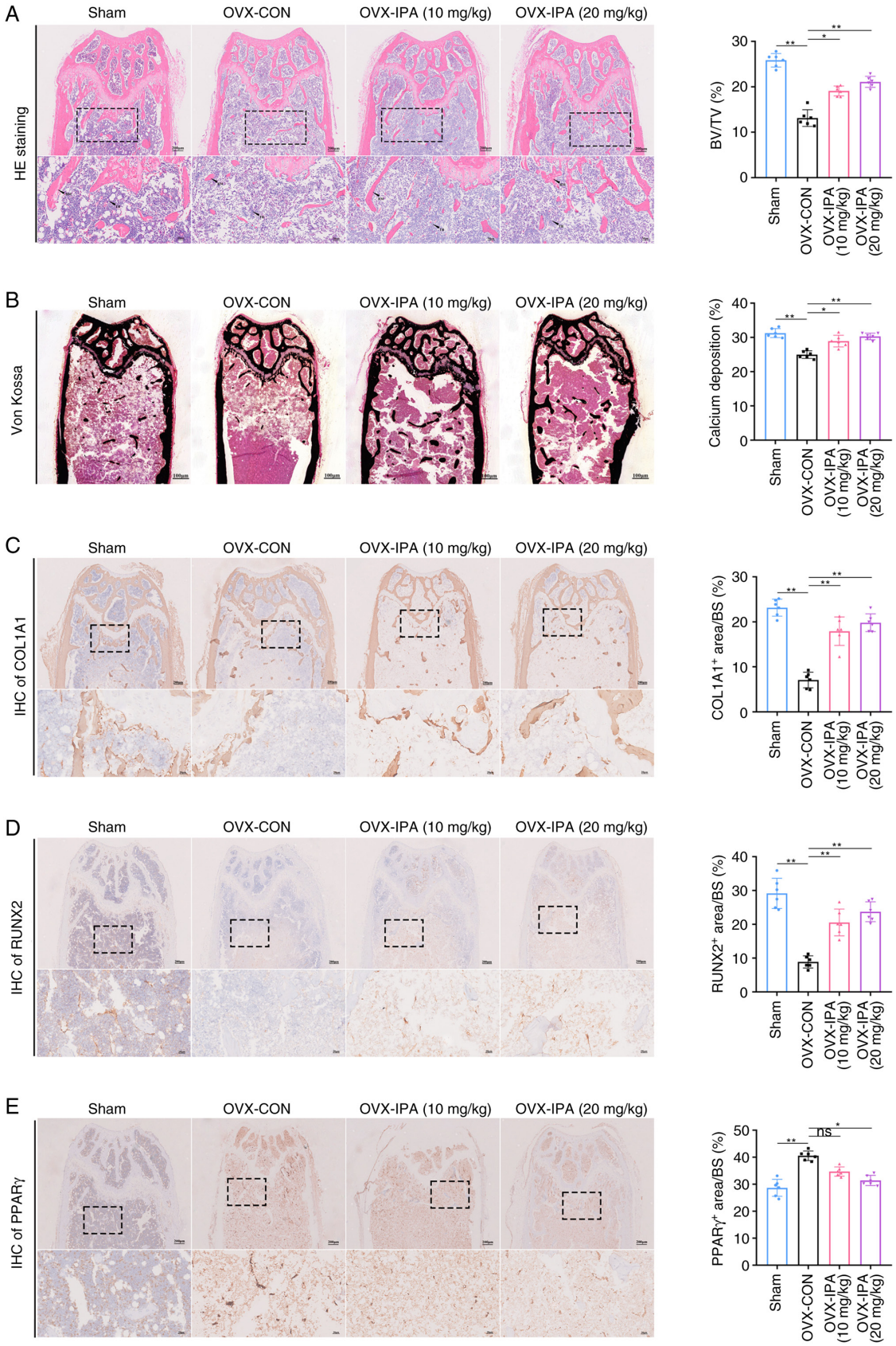

Figure 7. IPA supplementation suppresses PPARγ signalling to enhance bone formation and attenuate OVX-induced bone loss. (A) Representative H&E staining images and quantification of BV/TV in the four experimental groups. Scale bar, 200 μm. (B) Representative Von Kossa staining images and quantification of calcium deposition in the four groups. Scale bar, 100 μm. (C) Histological analysis of femoral tissue stained for COL1A1 and quantification of the COL1A1-positive area by IHC staining (n=6). (D) Histological analysis of femoral tissue stained for RUNX2 and quantification of the RUNX2-positive area by IHC staining (n=6). (E) Histological analysis of femoral tissue stained for PPARγ and quantification of the PPARγ-positive area by IHC staining (n=6). Data are presented as the mean ± SD. *P<0.05 and **P<0.01 compared with the control group. IPA, indole-3-propionic acid; PPARγ, peroxisome proliferator-activated receptor gamma; OVX, ovariectomy; COL1A1, collagen, type I, alpha 1; IHC, immunohistochemistry; RUNX2, Runt-related transcription factor 2; ns, not significant.

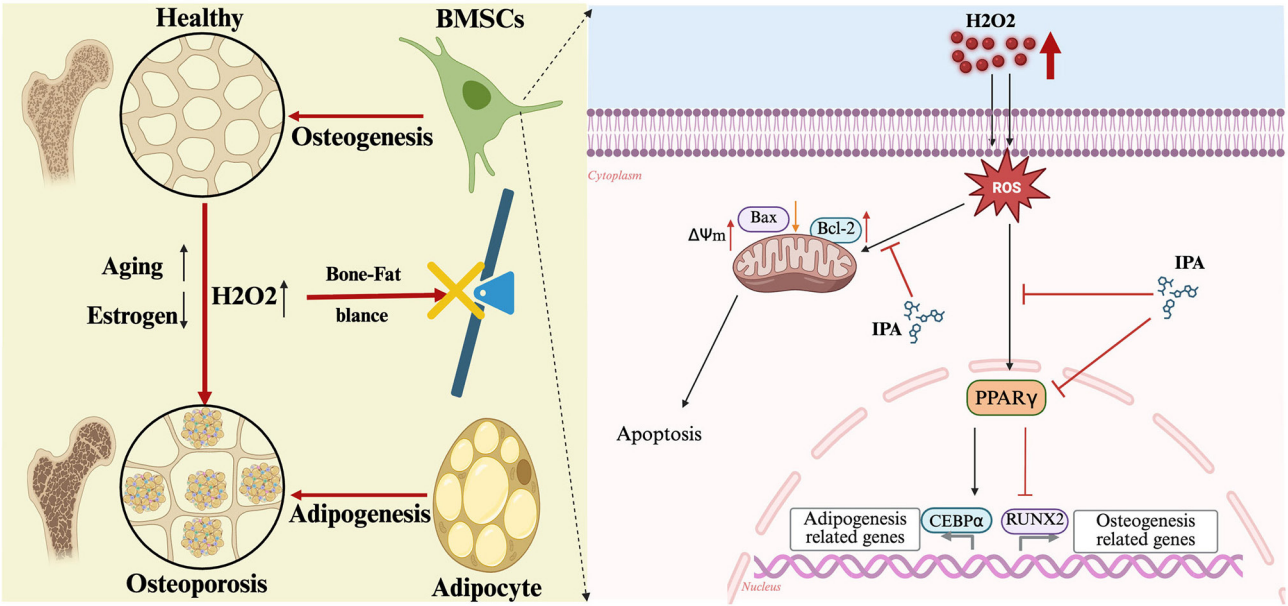

Figure 8. Schematic illustration of the proposed working model. BMSCs, bone marrow stromal cells; IPA, indole-3-propionic acid; PPARγ, peroxisome proliferator-activated receptor gamma; ROS, reactive oxygen species.

compared with the OVX group (Fig. 7E). Furthermore, no obvious pathological injury was observed in the heart, liver, spleen, lung, or kidney following oral IPA supplementation (Fig. S7). Collectively, these data demonstrated that IPA alleviates OP by suppressing PPARγ signalling, thereby restoring the osteogenic-adipogenic balance and promoting bone formation.

Discussion

In the present study, IPA, a gut microbiota-derived metabolite, was identified as a critical regulator of bone marrow lineage commitment and skeletal homeostasis. The present findings established a previously unrecognised mechanistic link between microbial metabolism and OP, demonstrating that IPA restores the osteogenic-adipogenic balance by suppressing PPARγ signalling. A schematic overview of the study is presented in Fig. 8. A key conceptual advance is the shift in focus from bone resorption-centred mechanisms toward the regulation of BMSC fate. Although previous studies have primarily highlighted the role of microbial metabolites in osteoclast activity, the present results demonstrated that IPA directly regulates mesenchymal lineage allocation. This distinction is important, as impaired osteogenesis, rather than excessive bone resorption, is increasingly recognised as a major contributor to age- and oestrogen deficiency-related bone loss.

In recent years, the role and mechanisms of the gut microbiota and its metabolites in the pathogenesis of OP have gradually gained recognition (28). It has been demonstrated that gut microbiota-derived metabolites exert significant regulatory effects on both osteoblasts and osteoclasts (25). Tryptophan is an essential amino acid (21). Undigested dietary tryptophan is metabolised by gut microbiota, including the *Clostridium* and *Bacteroides* genera, to produce indole and its derivatives. These indole derivatives constitute a distinct class of tryptophan metabolites produced exclusively through microbial tryptophan catabolism (44). Among them, IPA, a tryptophan-derived microbial metabolite predominantly produced by the *Clostridia* genus, has attracted increasing attention because of its involvement in metabolic regulation, inflammation, and gut barrier protection (26). In the present study, it was found that both *Clostridium* abundance and IPA levels were significantly reduced in OVX mice. Moreover, IPA levels were positively correlated with the abundance of the *Clostridium* genus, suggesting that reduced *Clostridium* abundance contributes to decreased IPA production. The observed association between reduced *Clostridium* abundance and decreased IPA levels is correlative. Further studies using microbiota manipulation or *Clostridium*-specific interventions are needed to confirm a direct causal relationship.

The results of the present study further demonstrated that IPA supplementation alleviated OP-associated bone loss. It has been shown that IPA derived from *Clostridium* inhibits osteoclast formation and that *Clostridium* abundance is decreased in OVX-induced OP mouse models (35), which is consistent with the present findings. Other studies reported that *Lactobacillus*-derived IPA and IAA levels were significantly decreased in OVX mice (34,36). These findings suggest that variations in intestinal microbiota composition among individuals may be influenced by host metabolism and environmental factors. Therefore, further multicentre studies with larger sample sizes are required to validate gut microbial alterations in OP populations. In addition, the present study only explored the therapeutic effects of oral IPA supplementation in OVX mice. The potential effects of supplementation with IPA-producing bacteria or faecal microbiota transplantation were not investigated and warrant further study in the future.

The present data further demonstrated that IPA acts as a context-dependent regulator that exerts minimal effects under physiological conditions but becomes highly active under oxidative stress. This characteristic suggests that IPA may selectively restore pathological imbalance without disrupting normal tissue homeostasis, representing a potential advantage over

conventional pharmacological agents. Mechanistically, PPARγ was identified as a central target of IPA. As a master regulator of adipogenesis, PPARγ plays a critical role in determining BMSC fate (45). Aberrant activation of PPARγ in OP promotes adipocyte formation at the expense of osteoblast differentiation. The current transcriptomic, biochemical and molecular docking analyses collectively support the notion that IPA suppresses PPARγ signalling, thereby reprogramming lineage commitment toward osteogenesis. These findings provide a mechanistic basis for targeting the bone-fat balance as a therapeutic strategy.

In addition to its effects on differentiation, IPA also exhibited cytoprotective properties by mitigating oxidative stress-induced apoptosis in BMSCs. Given that oxidative stress is a major driver of skeletal aging and oestrogen deficiency-associated bone loss (46,47), this dual function further strengthens the therapeutic potential of IPA. Importantly, the present *in vivo* findings demonstrated that oral administration of IPA significantly improved bone mass and microarchitecture without detectable systemic toxicity. These findings highlight the translational potential of microbiota-derived metabolites as safe and effective therapeutic agents.

The present study also had certain limitations. First, although the present findings strongly suggested that IPA regulates BMSC differentiation through the PPARγ signalling pathway, based on transcriptomic and molecular docking analyses, the detailed downstream molecular mechanisms linking PPARγ suppression to restored osteogenesis were not fully elucidated. In addition, several key pathways closely associated with osteogenesis and oxidative stress responses, including the Wnt/β-catenin, BMP/Smad, AMPK and NRF2 signalling pathways (45), were not investigated. Future studies employing genetic gain- and loss-of-function models, as well as pharmacological modulation of specific targets, are needed to clarify the precise molecular interactions underlying the effects of IPA. Second, although IPA supplementation improved bone mass in OVX mice, the broader framework of gut microbial modulation was not addressed. Because the abundance of *Clostridia* is strongly correlated with IPA levels, microbial interventions such as faecal microbiota transplantation, selective probiotic colonisation and dietary strategies that enhance IPA-producing bacteria may provide more sustained and physiological approaches for correcting the bone-fat imbalance associated with OP. The stability, colonisation efficiency and host-microbe interactions of *Clostridia* and other IPA-producing bacteria should therefore be further explored in future studies. Additionally, the present study demonstrated promising therapeutic effects of IPA *in vivo*. However, IPA was not compared with standard anti-osteoporotic drugs, and the study was limited to preclinical models. Future work should evaluate its comparative efficacy, safety, and translational potential.

In conclusion, IPA was identified as a key microbiota-derived regulator of bone-fat balance in OP. IPA restores skeletal homeostasis by reprogramming BMSC lineage commitment through suppression of PPARγ signalling and protection against oxidative stress. These findings uncover a previously unrecognised gut-bone metabolic axis and highlight IPA as a promising therapeutic strategy for OP.

Acknowledgements

Not applicable.

Funding

The present study was supported by the National Natural Science Foundation of China (grant nos. 81971160 and 82402806).

Availability of data and materials

The data generated in the present study may be found in the NCBI Sequence Read Archive under accession numbers PRJNA1327782 and PRJNA1371077 or at the following URL: https://www.ncbi.nlm.nih.gov/bioproject/PRJNA1327782; https://www.ncbi.nlm.nih.gov/bioproject/PRJNA1371077.

Authors' contributions

JB wrote the original draft, conducted investigation, developed methodology, curated data, and wrote, reviewed and edited the manuscript. RW wrote the original draft and developed methodology. JF conducted investigation, data curation and visualization. SS conducted formal analysis and data curation. GS developed methodology and curated data. QY and AS visualized and curated data. DH validated data and developed methodology. SG and FZ wrote, reviewed and edited the manuscript, validated data, conceptualized and supervised the study, and acquired funding. YL wrote, reviewed and edited the manuscript, validated data, conceptualized and supervised the study. All authors agree to be accountable for all aspects of work ensuring integrity and accuracy. All authors read and approved the final version of the manuscript. JB and FZ confirm the authenticity of all the raw data.

Ethics approval and consent to participate

All animal experiments were approved by the Peking University Third Hospital (approval no. BCAA0292; Beijing, China) and conducted in accordance with ARRIVE guidelines.

Patient consent for publication

Not applicable.

Competing interests

The authors declare that they have no competing interests.

References

1. Wang L, Yu W, Yin X, Cui L, Tang S, Jiang N, Cui L, Zhao N, Lin Q, Chen L, *et al*: Prevalence of osteoporosis and fracture in China: The China osteoporosis prevalence study. JAMA Netw Open 4: e2121106, 2021.
2. Curtis EM, Moon RJ, Dennison EM, Harvey NC and Cooper C: Recent advances in the pathogenesis and treatment of osteoporosis. Clin Med (Lond) 16: 360-364, 2016.
3. Rachner TD, Khosla S and Hofbauer LC: Osteoporosis: Now and the future. Lancet 377: 1276-1287, 2011.
4. Ayers C, Kansagara D, Lazur B, Fu R, Kwon A and Harrod C: Effectiveness and safety of treatments to prevent fractures in people with low bone mass or primary osteoporosis: A living systematic review and network meta-analysis for the american college of physicians. Ann Intern Med 176: 182-195, 2023.
5. Stegen S and Carmeliet G: Metabolic regulation of skeletal cell fate and function. Nat Rev Endocrinol 20: 399-413, 2024.

6. Zhang J, Hu W, Zou Z, Li Y, Kang F, Li J and Dong S: The role of lipid metabolism in osteoporosis: Clinical implication and cellular mechanism. Genes Dis 11: 101122, 2024.
7. Zou J, Chen H, Fan X, Qiu Z, Zhang J and Sun J: Garcinol prevents oxidative stress-induced bone loss and dysfunction of BMSCs through NRF2-antioxidant signaling. Cell Death Discov 10: 82, 2024.
8. Alves CH, Farrell E, Vis M, Colin EM and Lubberts E: Animal models of bone loss in inflammatory arthritis: From cytokines in the bench to novel treatments for bone loss in the Bedside-a comprehensive review. Clin Rev Allergy Immunol 51: 27-47, 2016.
9. Zhang W, Wu X, Li W, Zhang H, Wang Y, Xu J, Li W, Qin Y, Wu Z, Ge G, *et al*: Pinosylvin inhibits inflammatory and osteoclastogenesis via NLRP3 inflammasome. Adv Sci (Weinh) 12: e01532, 2025.
10. Costa AG, Cusano NE, Silva BC, Cremers S and Bilezikian JP: Cathepsin K: Its skeletal actions and role as a therapeutic target in osteoporosis. Nat Rev Rheumatol 7: 447-456, 2011.
11. Veis DJ and O'Brien CA: Osteoclasts, master sculptors of bone. Annu Rev Pathol 18: 257-281, 2023.
12. Riegger J, Schoppa A, Ruths L, Haffner-Luntzer M and Ignatius A: Oxidative stress as a key modulator of cell fate decision in osteoarthritis and osteoporosis: A narrative review. Cell Mol Biol Lett 28: 76, 2023.
13. Iantomasi T, Romagnoli C, Palmini G, Donati S, Falsetti I, Miglietta F, Aurilia C, Marini F, Giusti F and Brandi M: Oxidative stress and inflammation in osteoporosis: Molecular mechanisms involved and the relationship with microRNAs. Int J Mol Sci 24: 3772, 2023.
14. Akune T, Ohba S, Kamekura S, Yamaguchi M, Chung UI, Kubota N, Terauchi Y, Harada Y, Azuma Y, Nakamura K, *et al*: PPARgamma insufficiency enhances osteogenesis through osteoblast formation from bone marrow progenitors. J Clin Invest 113: 846-855, 2004.
15. Ahmadian M, Suh JM, Hah N, Liddle C, Atkins AR, Downes M and Evans RM: PPARgamma signaling and metabolism: The good, the bad and the future. Nat Med 19: 557-566, 2013.
16. Tsai YS and Maeda N: PPARgamma: A critical determinant of body fat distribution in humans and mice. Trends Cardiovasc Med 15: 81-85, 2005.
17. Tontonoz P and Spiegelman BM: Fat and beyond: The diverse biology of PPARgamma. Annu Rev Biochem 77: 289-312, 2008.
18. Liu C, Xiong Q, Li Q, Lin W, Jiang S, Zhang D, Wang Y, Duan X, Gong P and Kang N: CHD7 regulates bone-fat balance by suppressing PPAR-gamma signaling. Nat Commun 13: 1989, 2022.
19. Zhang YW, Song PR, Wang SC, Liu H, Shi ZM and Su JC: Diets intervene osteoporosis via gut-bone axis. Gut Microbes 16: 2295432, 2024.
20. Zhang YW, Wu Y, Liu XF, Chen X and Su JC: Targeting the gut microbiota-related metabolites for osteoporosis: The inextricable connection of gut-bone axis. Ageing Res Rev 94: 102196, 2024.
21. Al Saedi A, Sharma S, Summers MA, Nurgali K and Duque G: The multiple faces of tryptophan in bone biology. Exp Gerontol 129: 110778, 2020.
22. Xiang T, Yang C, Xie L, Xiao S, Tang Y, Huang G, Sun D, Chen Y and Luo F: Aberrant tryptophan metabolism manipulates osteochondral homeostasis. Research (Wash D C) 8: 0728, 2025.
23. Miao H, Zhang SJ, Wu X, Li P and Zhao YY: Tryptophan metabolism as a target in gut microbiota, ageing and kidney disease. Int J Biol Sci 21: 4374-4387, 2025.
24. Chen Y, Yang C, Deng Z, Xiang T, Ni Q, Xu J, Sun D and Luo F: Gut microbially produced tryptophan metabolite melatonin ameliorates osteoporosis via modulating SCFA and TMAO metabolism. J Pineal Res 76: e12954, 2024.
25. Su S and Tian L: Association between dietary tryptophan intake and bone health: A cross-sectional study. Calcif Tissue Int 116: 6, 2024.
26. Xu H, Luo Y, An Y and Wu X: The mechanism of action of indole-3-propionic acid on bone metabolism. Food Funct 16: 406-421, 2025.
27. Kim CS, Jung S, Hwang GS and Shin DM: Gut microbiota indole-3-propionic acid mediates neuroprotective effect of probiotic consumption in healthy elderly: A randomized, double-blind, placebo-controlled, multicenter trial and in vitro study. Clin Nutr 42: 1025-1033, 2023.
28. Anaya JM, Bollag WB, Hamrick MW and Isales CM: The role of tryptophan metabolites in musculoskeletal stem cell aging. Int J Mol Sci 21: 6670, 2020.
29. Li J, Zhang L, Wu T, Li Y, Zhou X and Ruan Z: Indole-3-propionic acid improved the intestinal barrier by enhancing epithelial barrier and mucus barrier. J Agric Food Chem 69: 1487-1495, 2021.
30. Zeng Y, Guo M, Wu Q, Tan X, Jiang C, Teng F, Chen J, Zhang F, Ma X, Li X, *et al*: Gut microbiota-derived indole-3-propionic acid alleviates diabetic kidney disease through its mitochondrial protective effect via reducing ubiquitination mediated-degradation of SIRT1. J Adv Res 73: 607-630, 2025.
31. Zhao ZH, Xin FZ, Xue Y, Hu Z, Han Y, Ma F, Zhou D, Liu XL, Cui A, Liu Z, *et al*: Indole-3-propionic acid inhibits gut dysbiosis and endotoxin leakage to attenuate steatohepatitis in rats. Exp Mol Med 51: 1-14, 2019.
32. Wu R, Kong Y, Li J, Chen H, Jiao Y, Sun C and Ju Y: Indole-3 propionate inhibits NF-kappaB/NLRP3-mediated osteoclastogenesis and improves bone quality in high-fat-diet induced obese mice. Biochim Biophys Acta Mol Basis Dis 1871: 167952, 2025.
33. Bai J, Si G, Wang R, Su S, Fan J, He X, Lv Y, Gao S and Zhou F: Gut metabolite indoleacrylic acid suppresses osteoclast formation by AHR mediated NF-κB signaling pathway. Int J Biol Sci 22: 951-969, 2026.
34. Bai J, Han G, Fan J, Wang R, Su S, Sun A, Hu D, Lv Y, Gao S and Zhou F: Gut microbial metabolite alleviates osteoporosis by attenuating AKT-NFATc1 signaling pathway and ROS production. Free Radic Biol Med 243: 351-366, 2026.
35. Peng R, Song C, Gou S, Liu H, Kang H, Dong Y, Xu Y, Hu P, Cai K, Feng Q, *et al*: Gut *Clostridium sporogenes*-derived indole propionic acid suppresses osteoclast formation by activating pregnane X receptor. Pharmacol Res 202: 107121, 2024.
36. Chen C, Cao Z, Lei H, Zhang C, Wu M, Huang S, Li X, Xie D, Liu M, Zhang L and Chen G: Microbial tryptophan metabolites ameliorate Ovariectomy-induced bone loss by repairing intestinal AhR-mediated gut-bone signaling pathway. Adv Sci (Weinh) 11: e2404545, 2024.
37. Bai J, Zhang W, Zhou C, Zhao G, Zhong H, Hang K, Xu J, Zhang W, Chen E, Wu J, *et al*: MFG-E8 promotes osteogenic differentiation of human bone marrow mesenchymal stem cells through GSK3β/β-catenin signaling pathway. FASEB J 37: e22950, 2023.
38. Wu X, Wang K, Chen H, Cao B, Wang Y, Wang Z, Dai C, Yao M, Ji X, Jiang X, *et al*: Hypoxia-induced mitochondrial fission regulates the fate of bone marrow mesenchymal stem cells by maintaining HIF1α stabilization. Free Radic Biol Med 225: 127-144, 2024.
39. Jurisic V, Srdic-Rajic T, Konjevic G, Bogdanovic G and Colic M: TNF-α induced apoptosis is accompanied with rapid CD30 and slower CD45 shedding from K-562 cells. J Membr Biol 239: 115-122, 2011.
40. Liu Y, Yang X, Gan J, Chen S, Xiao ZX and Cao Y: CB-Dock2: Improved protein-ligand blind docking by integrating cavity detection, docking and homologous template fitting. Nucleic Acids Res 50: W159-W164, 2022.
41. Li D, Zhao Z, Zhu L, Feng H, Song J, Fu J, Li J, Chen Z and Fu H: 7,8-DHF inhibits BMSC oxidative stress via the TRKB/PI3K/AKT/NRF2 pathway to improve symptoms of postmenopausal osteoporosis. Free Radic Biol Med 223: 413-429, 2024.
42. Chen M, Liang H, Wu M, Ge H, Ma Y, Shen Y, Lu S, Shen C, Zhang H, Wang Z and Tang L: Fgf9 regulates bone marrow mesenchymal stem cell fate and bone-fat balance in osteoporosis by PI3K/AKT/Hippo and MEK/ERK signaling. Int J Biol Sci 20: 3461-3479, 2024.
43. Yang L, Liu X, Chen S, Sun J, Tao Y, Ma L, Zeng Y, Luo K, Tian R and Meng X: Scutellarin ameliorates mitochondrial dysfunction and apoptosis in OGD/R-insulted HT22 cells through mitophagy induction. Biomed Pharmacother 179: 117340, 2024.
44. Zhao J, Bai X, Du J, Chen Y, Guo X, Zhang J, Gan J, Wu P, Chen S, Zhang X, *et al*: Tryptophan metabolism: From physiological functions to key roles and therapeutic targets in cancer (Review). Oncol Rep 54: 86, 2025.
45. Li Y, Jin D, Xie W, Wen L, Chen W, Xu J, Ding J and Ren D: PPAR-γ and wnt regulate the differentiation of MSCs into adipocytes and osteoblasts respectively. Curr Stem Cell Res Ther 13: 185-192, 2018.
46. Kim K, Kim JH, Kim I, Seong S, Koh JT and Kim N: Sestrin2 inhibits RANKL-induced osteoclastogenesis through AMPK activation and ROS inhibition. Free Radic Biol Med 211: 77-88, 2024.
47. Ye W, Liao Y, Liu X, Wang Y, Li T, Zhao Y, He Z, Chen J, Yin M, Sheng Y, *et al*: Dectin-2 depletion alleviates osteoclast-induced bone loss in periodontitis via Syk/NOX2/ROS signaling. Free Radic Biol Med 229: 13-29, 2025.